

# Toward High Energy Density All Solid-State Sodium Batteries with Excellent Flexibility

Yu Yao, Zhenyao Wei, Haiyun Wang, Huijuan Huang, Yu Jiang, Xiaojun Wu, Xiayin Yao,\* Zhong-Shuai Wu,\* and Yan Yu\*

Dedicated to Prof. Joachim Maier on the occasion of his 65th birthday

All solid-state sodium batteries (ASSBs) have attracted considerable attention due to their enhanced safety, long lifespan, and high energy density. However, several challenges have plagued the development of ASSBs, especially the relatively low ionic conductivity of solid-state electrolytes (SSEs), large interfacial resistance, and low stability/compatibility between SSEs and electrodes. Here, a high-performance all solid-state sodium battery (NVP@C|PEGDMA-NaFSI-SPE|Na) is designed by employing carbon coated  $\text{Na}_3\text{V}_2(\text{PO}_4)_3$  composite nanosheets (NVP@C) as the cathode, solvent-free solid polymer electrolyte (PEGDMA-NaFSI-SPE) as the electrolyte and metallic sodium as the anode. The integrated electrolyte and cathode system prepared by the in situ polymerization process exhibits high ionic conductivity ( $\approx 10^{-4} \text{ S cm}^{-1}$  at room temperature) and an outstanding electrolyte/electrode interface. Benefiting from these merits, the soft-pack ASSB (NVP@C|PEGDMA-NaFSI-SPE|Na) delivers excellent cycling life over 740 cycles (capacity decay of only 0.007% per cycle) and maintains 95% of the initial reversible capacity with almost no self-discharge even after resting for 3 months. Moreover, the bendable ASSB exhibits a high capacity of  $106 \text{ mAh g}^{-1}$  (corresponds to energy density of  $\approx 355 \text{ Wh kg}^{-1}$ ) at  $0.5 \text{ C}$  despite undergoing repeated bending for 535 cycles. This work offers a new strategy to fabricate high-performance flexible ASSBs with a long lifespan and excellent flexibility.

to utilize energy storage systems that are safe and cost-effective.<sup>[1–3]</sup> Sodium-ion batteries (SIBs) with similar charge storage mechanisms to lithium-ion batteries have been considered as economic alternatives for large-scale energy storage systems because of the abundant sodium reserve in earth.<sup>[4–6]</sup> Nevertheless, traditional SIBs are suffering from potential safety hazards derived from the high flammability and leakage of organic liquid electrolytes. Recently, rechargeable all solid-state sodium batteries (ASSBs) have captured widespread attention for the next generation of energy storage devices.<sup>[7,8]</sup> On one hand, ASSBs could address the safety issues of batteries including the flammability and leakage of liquid electrolytes, which will inevitably accelerate the commercialization process.<sup>[9–11]</sup> On the other hand, the use of sodium (Na) metal with a high theoretical capacity ( $1166 \text{ mAh g}^{-1}$ ) and low redox potential ( $-2.71 \text{ V}$  versus the standard hydrogen potential) as anode for the ASSB results in wider output voltage and higher energy density.<sup>[12,13]</sup> However, the development of ASSBs is hindered by several intractable issues associated with

both solid-state electrolytes (SSEs) and electrode materials.<sup>[14]</sup> First, the low ionic conductivity of SSEs at room temperature (RT) and poor electronic conductivity resulting from the insufficient interfacial contact between the electrode and electrolyte

## 1. Introduction

To meet the requirements of integrating intermittent energy sources (i.e., wind, solar energy) into smart grid, it is urgent

Y. Yao, H. Wang, H. Huang, Dr. Y. Jiang, Prof. X. Wu, Prof. Y. Yu  
Hefei National Laboratory for Physical Sciences at the Microscale  
Department of Materials Science and Engineering  
CAS Key Laboratory of Materials for Energy Conversion  
University of Science and Technology of China  
Hefei, Anhui 230026, China  
E-mail: yanyumse@ustc.edu.cn

Z. Wei, Prof. X. Yao  
Ningbo Institute of Materials Technology & Engineering  
Chinese Academy of Sciences (CAS)  
Ningbo 315201, China  
E-mail: yaoyx@nimte.ac.cn

 The ORCID identification number(s) for the author(s) of this article can be found under <https://doi.org/10.1002/aenm.201903698>.

Prof. Z.-S. Wu  
Dalian National Laboratory For Clean Energy  
Dalian Institute of Chemical Physics  
Chinese Academy of Sciences  
457 Zhongshan Road, Dalian 116023, China  
E-mail: wuzs@dicp.ac.cn

Prof. Y. Yu  
Dalian National Laboratory for Clean Energy (DNL)  
Chinese Academy of Sciences (CAS)  
457 Zhongshan Road, Dalian, Liaoning, China

Prof. Y. Yu  
State Key Laboratory of Fire Science  
University of Science and Technology of China  
Hefei, Anhui 230026, China

DOI: 10.1002/aenm.201903698

lead to high interfacial resistance ( $R$ ).<sup>[15,16]</sup> Second, the chemical/electrochemical instability of electrode materials and SSEs result in the electrochemical degradation.<sup>[17]</sup> Finally, the large volume change of electrode materials during the  $\text{Na}^+$  insertion/extraction process causes stress to the electrode, leading to rapid capacity fading.<sup>[18]</sup> Therefore, it is highly desired to develop advanced ASSB system by rational component optimization and interfacial modification of the SSE and electrode materials to pursue high energy density and long cycle life.

Many efforts have been made to exploit various solid-state electrolytes that include solid polymer electrolytes (SPEs) and inorganic ceramic electrolytes (ICEs).<sup>[9,19–21]</sup> The ICEs (i.e., garnet, NASICON, perovskite, and sulfides-type materials) usually exhibit considerable ionic conductivity ( $>10^{-4}$  S  $\text{cm}^{-1}$  at RT), good thermal stability and robust mechanical strength.<sup>[22,23]</sup> However, the intrinsic high roughness and rigidity of ICEs will cause poor contact with electrode materials and difficulties in the processing, leading to high contact resistance and manufacturing cost.<sup>[24,25]</sup> Compared with inorganic electrolyte, SPEs exhibit better mechanical flexibilities and more favorable interfacial contact with electrodes, which could compensate the volume change of electrode materials and make them promising candidates for flexible ASSBs.<sup>[26–28]</sup> SPEs generally consist of sodium salts (including sodium bis(trifluoromethanesulfonyl) imide (NaTFSI), sodium bis(fluorosulfonyl)imide (NaFSI), or sodium perchlorate ( $\text{NaClO}_4$ )) and polymer matrix (such as poly(ethyleneoxide) (PEO), polyacrylonitrile, poly(vinylidene fluoride), or poly(methyl methacrylate)), where sodium salt is sodium source and polymer matrix acts as the  $\text{Na}^+$  transporting host.<sup>[29–32]</sup> The viability of NaFSI as an ideal salt has been exemplified in the literature because it can control the reaction with the solvent due to its unstable S–F bond.<sup>[24,33]</sup> As for the polymer matrixes, PEO-based material is regarded as the most promising one by virtue of its good structural and chemical stability and high solubility for sodium salts.<sup>[34,35]</sup> Nevertheless, the poor mechanical property, low oxidation potential, and high crystallinity of PEO lead to a low ionic conductivity ( $\approx 10^{-6}$  S  $\text{cm}^{-1}$  at RT), which severely restricts its further practical applications.<sup>[36]</sup> In addition, conventional solution casting method for SPEs membranes may lead to low Coulombic efficiencies (CE) and irreversible side reactions of the ASSBs due to residual liquid solvent in the SPEs.<sup>[37,38]</sup> And this technique is complicated, high-cost, and environmentally unfriendly.<sup>[39]</sup> Recently, the solvent-free UV-curing method for SPEs preparation has been demonstrated to be a facile and cost-effective approach for large-scale fabrication due to its low operating temperature and fast reaction rate.<sup>[27,29,40]</sup>

For the high-performance ASSBs, stable operation of the battery system also heavily relies on the cathode materials.  $\text{Na}_3\text{V}_2(\text{PO}_4)_3$  (NVP) cathode shows numerous advantages as the sodium super ionic conductor: 1) high energy density ( $\approx 400$  Wh  $\text{kg}^{-1}$ ) derived from the high output voltage ( $\approx 3.4$  V versus  $\text{Na}/\text{Na}^+$ ); 2) stable structure during charge/discharge (only 8% volume change); 3) good thermal stability.<sup>[41,42]</sup> Nevertheless, the intrinsic poor electrical conductivity of NVP dampens the electrochemical performance as the electrode material.<sup>[43]</sup> Some strategies have been employed for NVP to enhance the performance, for example, by downsizing the NVP particle size to shorten the  $\text{Na}^+$  diffusion distance, modifying

the NVP surface by a carbon layer to enhance the electronic conductivity, and designing 3D continuous electrode architecture to facilitate the transport of  $\text{Na}^+$  and electron.<sup>[18,44,45]</sup>

It should be noted that the bottleneck of ASSBs is no longer simply exploiting advanced electrode and SSE materials, but designing an effective solid–solid interface of the electrode material and SSE. The insufficient contact area of electrode and SSE would lead to a large interface resistance and poor electrochemical performance. Although SPEs present better electrolyte/electrode interfacial contact than that of ICEs in ASSBs because of the superior mechanical flexibilities, the electrolyte/electrode interface is still a severe problem, which restricts the development of ASSBs. Therefore, many factors should be fully taken into account to enhance the interfacial contact for improving the performance of ASSBs.

Herein, we design an advanced all solid-state sodium battery (NVP@C|PEGDMA-NaFSI-SPE|Na) by using carbon-coated  $\text{Na}_3\text{V}_2(\text{PO}_4)_3$  (NVP@C) as the cathode, UV-cured novel solid polymer electrolyte (PEGDMA-NaFSI-SPE) as the electrolyte and metallic sodium as the anode. In this ASSB, an effective integrated system of the electrolyte and cathode is prepared by in situ solvent-free polymerization process, resulting in the improved ionic conductivity ( $\approx 10^{-4}$  S  $\text{cm}^{-1}$  at RT) of the SSE and the enhanced interfacial contact of SSE and electrode materials. The sodium symmetrical battery (Na|PEGDMA-NaFSI-SPE|Na) confirms the significant suppression of Na dendrite growth and excellent electrochemical stability. The NVP@C cathode presents flower-like structure assembled by the 2D nanoplates, which could shorten the transport distance of Na ion and electron. The surface modification by carbon layer for NVP enhances the electronic conductivity and avoids the side reactions. Combined these merits, the advanced ASSB exhibits excellent reversible capacity of 102 mAh  $\text{g}^{-1}$  at 0.5 C after 740 cycles (capacity decay of only 0.007% per cycle) at 60 °C in a soft-pack battery. More impressively, this soft-pack battery could keep high capacity retention with almost no self-discharge behavior even after resting for 3 months. Besides, the bendable soft-pack ASSB (NVP@C|PEGDMA-NaFSI-SPE|Na) could deliver high reversible capacity of 106 mAh  $\text{g}^{-1}$  after 535 cycles at 0.5 C despite undergoing repeated bending at different stages and low electrochemical impedance in both flat and folding states. The outstanding electrochemical behaviors of the soft-pack ASSB are derived from the high ionic conductivity, good mechanical flexibilities, and low diffusion energy barrier of  $\text{Na}^+$  of the battery system, which are supported by the experimental results and DFT calculations.

The NVP@C cathode was prepared by rationally optimizing the nanostructured NASICON structure material (See the crystal structure of NVP in Figure 1a) via a facile solution method, realizing the 2D thin nanoplates assembled 3D flower-like structure.<sup>[45]</sup> As the vital component of ASSB, the solid-state electrolyte can be simultaneously served as separator and electrolyte. The solid polymer electrolyte (PEGDMA-NaFSI-SPE) was prepared by in situ solvent-free UV-cured method, as shown in Figure S1, Supporting Information, where the monomer precursor of the poly(ethylene glycol) methyl ether methacrylate (PEGDMA) and NaFSI were polymerized with 2,2-dimethoxy-2-phenylacetophenone (DMPA, 1 wt%) as the photoinitiator. To fabricate a good interfacial contact between

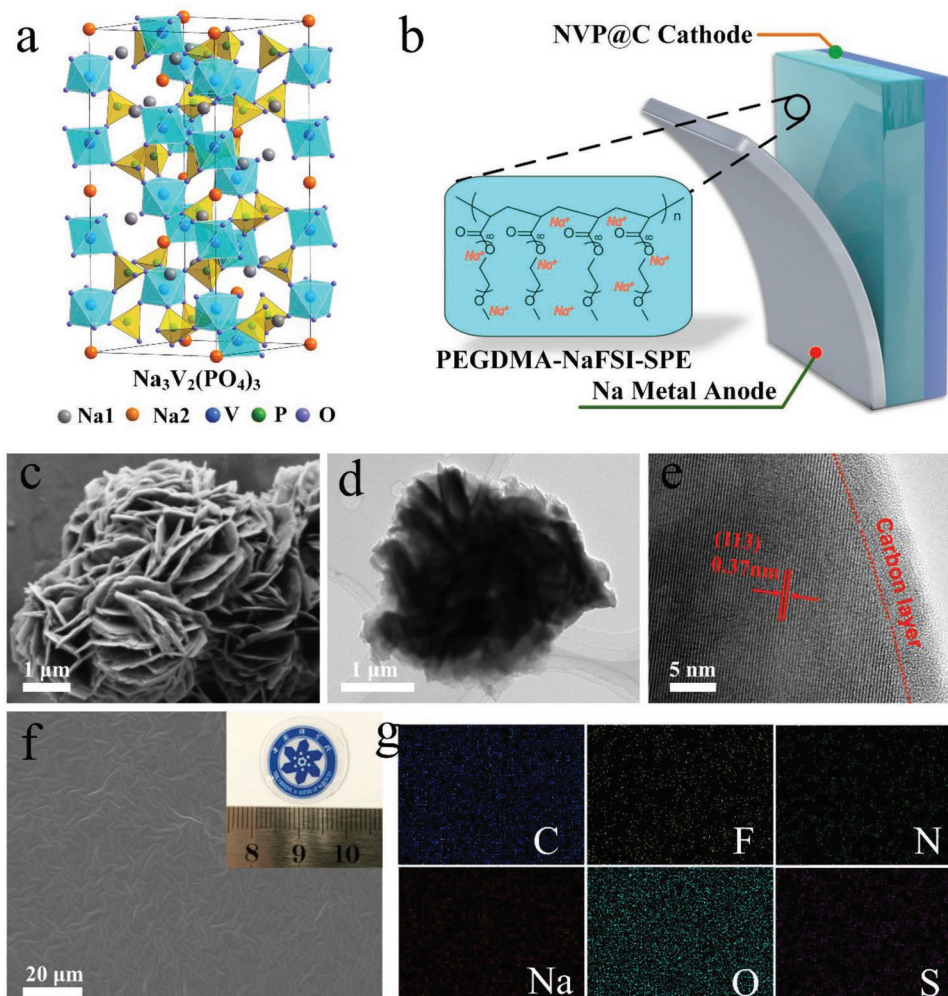


**Figure 1.** a) Crystal structure of  $\text{Na}_3\text{V}_2(\text{PO}_4)_3$  (NVP). b) The construction architecture of the NVP@C|PEGDMA-NaFSI-SPE|Na. c) SEM, d) TEM and e) HRTEM images of the NVP@C. f) SEM image and the digital photo, g) EDS element mappings of the PEGDMA-NaFSI-SPE.

SSE and cathode material, an integrated system of PEGDMA-NaFSI-SPE electrolyte and NVP@C cathode (see Figure 1b) was fabricated by penetrating the liquid monomer precursor into the cathode layer at RT, which undoubtedly enhance the solid–solid interface of electrolyte and electrode.<sup>[40]</sup> Finally, the all solid-state sodium battery (NVP@C|PEGDMA-NaFSI-SPE|Na) was assembled by employing the integrated electrolyte and cathode system with sodium metal as the anode, as shown in Figure 1b.

The morphology and structural characterization of the as-prepared samples are investigated by the scanning electron microscopy (SEM) and transmission electron microscopy (TEM). As shown in Figure 1c,d, the NVP@C presents flower-like structure which consists of the nanosheets. The average thickness of the nanosheet is around 27 nm. The 3D interconnected structure of NVP@C could significantly facilitate the chemical diffusion of  $\text{Na}^+$  and relieve mechanical stress caused by  $\text{Na}^+$  extraction/insertion.

According to the high-resolution transmission electron microscopy (HRTEM) image in Figure 1e, the clear lattice fringe with d-spacing of 0.37 nm for NVP@C corresponds

to the (113) plane of NVP.<sup>[46]</sup> And the carbon layer coated on the surface of the NVP@C is about 4 nm. Element mappings in Figure S2, Supporting Information, confirm the uniform distribution of C, Na, V, P, and O species in the NVP@C. As presented in Figure 1f and Figure S3, Supporting Information, the PEGDMA-NaFSI-SPE membrane shows transparent feature and excellent mechanical flexibility with a thickness of around 150  $\mu\text{m}$ . SEM image of the PEGDMA-NaFSI-SPE electrolyte (Figure 1f) displays a dense wrinkled surface without any pores. The diameter of PEGDMA-NaFSI-SPE membrane illustrated in Figure 1f is 18 mm. EDS element mappings of the PEGDMA-NaFSI-SPE indicate the homogeneous distribution of C, F, N, Na, O and S components (Figure 1g). X-ray diffraction (XRD) pattern demonstrates the typical rhombohedral NASICON structure of NVP@C with highly crystalline phase (Figure S4, Supporting Information).<sup>[47]</sup> No typical graphitic diffraction peaks could be observed, indicating amorphous state of the thin carbon layer. The carbon content of the NVP@C is determined to be 6.1 wt% by the Elementar vario EL cube. Raman spectrum of the NVP@C exhibits two strong peaks at 1357.9 and 1595.8 eV, which are assigned to the D and G band

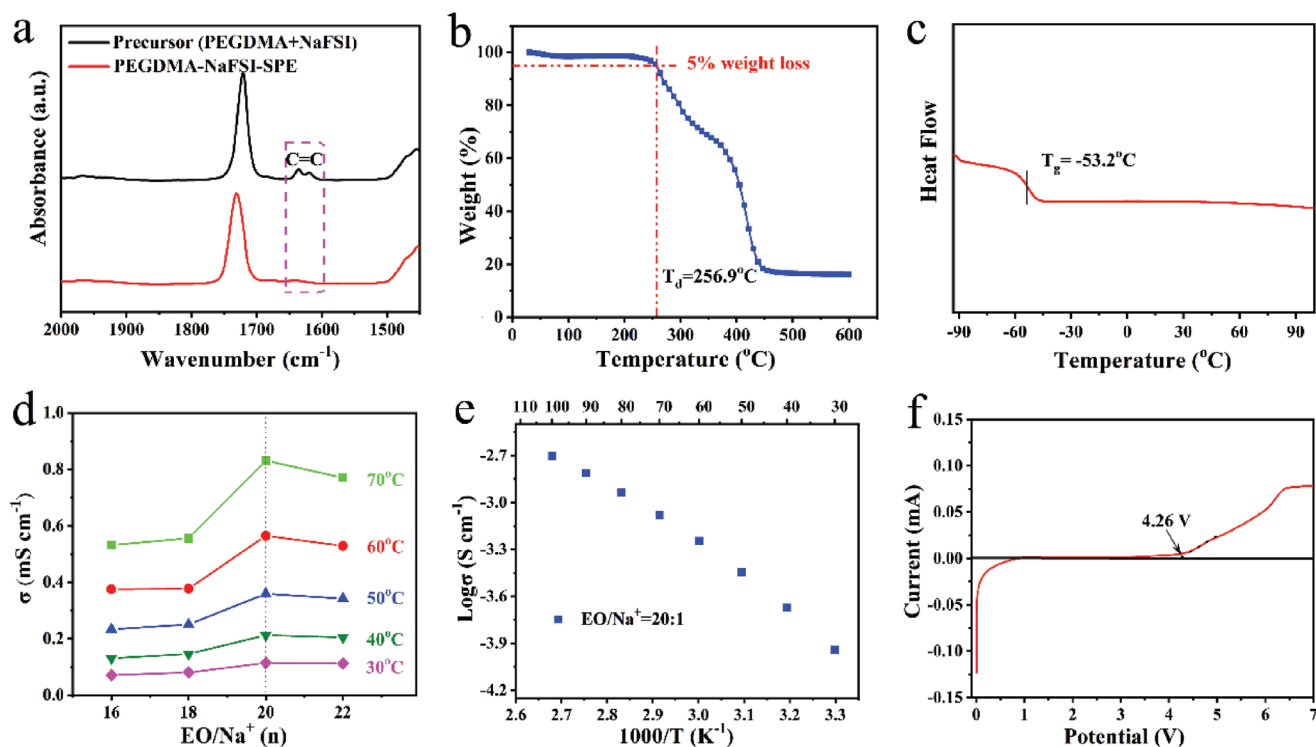


**Figure 2.** a) The partial enlarged FT-IR spectra of precursor solution and the as-prepared PEGDMA-NaFSI-SPE. b) TGA and c) DSC curves of the PEGDMA-NaFSI-SPE. d) The relationship between ionic conductivity and different mole ratio of EO/Na<sup>+</sup> at different temperatures, e) the relationship between ionic conductivity and temperature with mole ratio of EO/Na<sup>+</sup> = 20:1 for the PEGDMA-NaFSI-SPE. f) LSV curve of the PEGDMA-NaFSI-SPE at a sweep rate of 1 mV s<sup>-1</sup>.

of graphitic carbon, respectively (Figure S5, Supporting Information). The D and G band ( $I_D/I_G$ ) ratio of 0.93 is indicative of the disordered state of the carbon layer, which is well consistent with the HRTEM and XRD results.<sup>[43]</sup> X-ray photoelectron spectroscopy (XPS) demonstrates the existence of Na, O, V, C, and P elements in the NVP@C (Figure S6a, Supporting Information). In Figure S6b, Supporting Information, the peaks situated at 289.4, 286.3, 285.1, and 284.7 eV in C1s spectrogram could be attributed to O–C=O, C=O, C–O and C=C bonds, respectively.<sup>[42]</sup>

The physicochemical properties of the PEGDMA-NaFSI-SPE membrane were investigated by the systematic characterizations. The successful UV-polymerization of precursors is confirmed by the FT-IR spectra (Figure 2a and Figure S7, Supporting Information). No typical group of carbon–carbon double bond at around 1625 cm<sup>-1</sup> is observed in the as-prepared PEGDMA-NaFSI-SPE after the UV-cured process, indicating the absence of the PEGDMA monomer.<sup>[48]</sup> As shown in Figure S8, Supporting Information, the only broad peak of the PEGDMA-NaFSI-SPE at around 20° in XRD patterns demonstrates its amorphous feature, which is beneficial for ion transport in polymer host.<sup>[49]</sup> Figure 2b presents the thermogravimetric analysis (TGA) result, where the PEGDMA-NaFSI-SPE remains stable until 256.9 °C before it undergoes any decomposition and reaches about 5 wt% weight loss at the end of the measurement, indicating its excellent thermal stability. The glass transition temperature ( $T_g$ ) of PEGDMA-NaFSI-SPE membrane is around -53.2 °C and no endothermic peak can be observed

according to Figure 2c. It demonstrates the SSE exists in a totally amorphous state, which could greatly facilitate its chain segments movement and enhance the ionic conductivity.<sup>[29]</sup>

Understanding ionic transport mechanism is beneficial to design the SSEs with high ionic conductivity. For the SPEs, Na<sup>+</sup> can coordinate with the polar groups (such as –O–) on the segmental chains. With the movement of polymer segmental chains, Na<sup>+</sup> can continuously hop from one coordinating site to another and realize rapid ions transport. The mole ratio of EO/Na<sup>+</sup> could significantly impact the ionic conductivity of the SPEs.<sup>[50]</sup> Figure 2d exhibits ionic conductivities of the PEGDMA-NaFSI-SPE with different mole ratios ranging from 16 to 22 at different temperatures. Notably, the ionic conductivity of the PEGDMA-NaFSI-SPE increases with temperature. All of these SPEs present much higher ionic conductivity values at the mole ratio of EO/Na<sup>+</sup>(20:1) at different temperatures. The ionic conductivity of the PEGDMA-NaFSI-SPE at 60 and 30 °C with the EO/Na<sup>+</sup> of 20:1 is  $5.6 \times 10^{-4}$  and  $1.1 \times 10^{-4}$  S cm<sup>-1</sup>, respectively, which is much higher than those of the PEO-based SSEs ( $\approx 10^{-6}$  S cm<sup>-1</sup>).<sup>[40]</sup> Besides, the temperature dependence of ionic conductivities in the SPE was surveyed, as shown in Figure 2e. The ionic conductivity of the SPE follows the Vogel–Tammann–Fulcher (VTF) equation<sup>[36]</sup> as follows:

$$\sigma = AT^{-1/2} \exp(-E_a/k(T - T_0)) \quad (1)$$

where  $\sigma$  represents the ionic conductivity,  $A$  stands for a preexponential factor,  $E_a$  is the activation energy of sodium

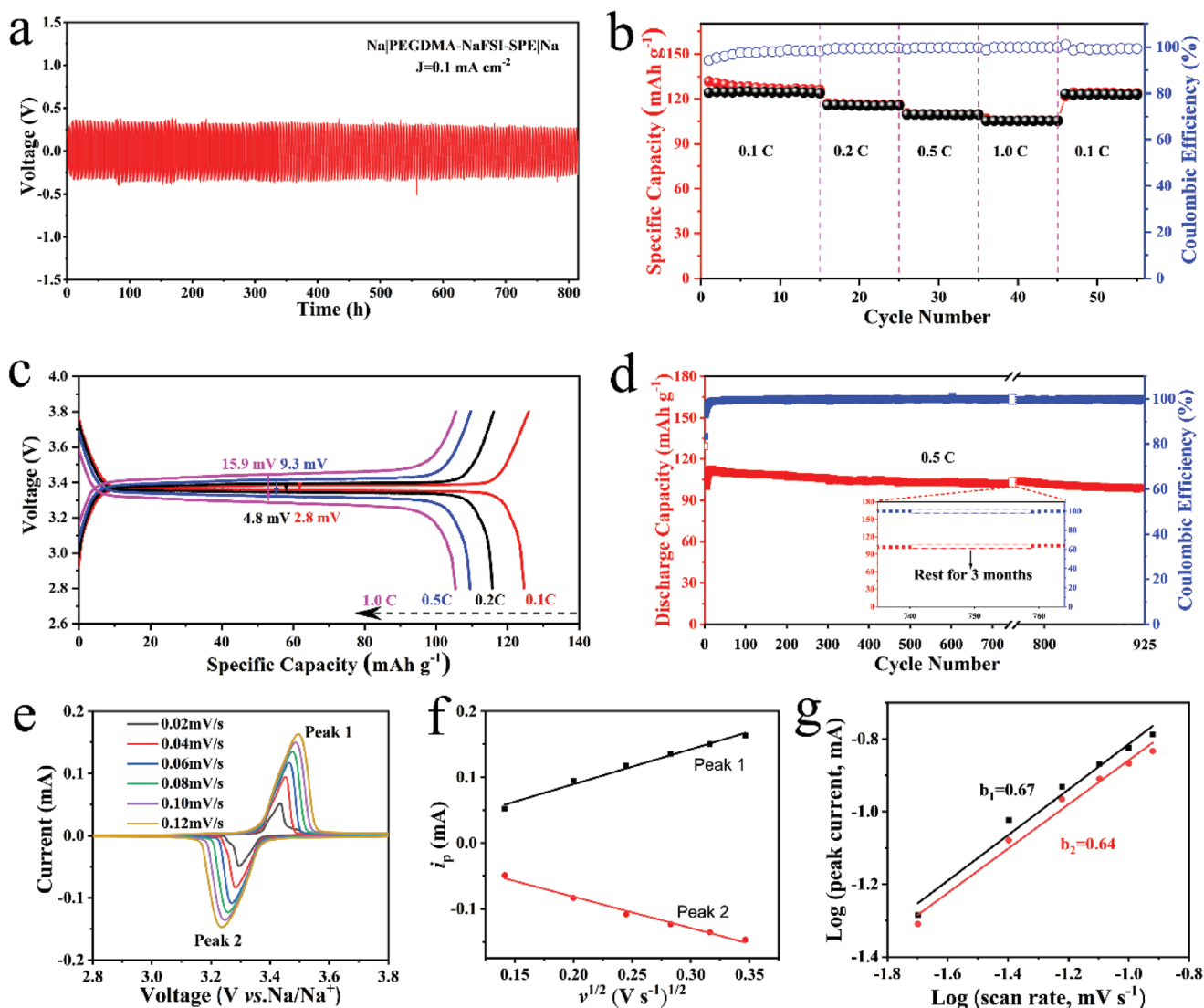


**Figure 3.** a) Chronopotentiometry curves of the Na|PEGDMA-NaFSI-SPE|Na symmetrical cell at  $0.1 \text{ mA cm}^{-2}$ . b) Rate capability, c) the corresponding voltage profiles obtained at different current densities and d) cycling stability at  $0.5 \text{ C}$  of the NVP@C|PEGDMA-NaFSI-SPE|Na. e) CV curves tested at various sweep rates, f) the corresponding relationship between peak currents and the square root of sweep rate ( $v^{1/2}$ ), g) the linear fitting plots of the transformed peak currents versus scan rates of the NVP@C|PEGDMA-NaFSI-SPE|Na.

conduction,  $k$  is the Boltzmann constant, and  $T_0$  is a parameter correlated to the glass transition temperature.  $E_a$  of the PEGDMA-NaFSI-SPE is  $0.045 \text{ eV}$  determined by the Equation (1), which is much lower than that of the PEO-based SSEs (Figure S9, Supporting Information).<sup>[40]</sup> The low activation energy and high ionic conductivity benefit from the comb-like side chains structure and more free volume for  $\text{Na}^+$  diffusion, which can significantly reduce the concentration of ion polarization in ASSBs.<sup>[40]</sup> Electrochemical stability of the PEGDMA-NaFSI-SPE was investigated in order to select electrode material and determine the working voltage of batteries. Linear sweep voltammograms (LSV) curve in Figure 2f exhibits no oxidation peak up to  $4.26 \text{ V}$  (versus  $\text{Na}/\text{Na}^+$ ), which indicates the superior electrochemical stability and the possibility for matching high-voltage cathode material of the PEGDMA-NaFSI-SPE.

The dynamic stability and electrochemical compatibility of the interface between the PEGDMA-NaFSI-SPE electrolyte and metallic Na electrode were measured in a symmetric cell of Na|PEGDMA-NaFSI-SPE|Na at  $60 \text{ }^\circ\text{C}$ . The symmetric cell exhibits a smooth potential with excellent sodium plating/stripping behavior at current density of  $0.1 \text{ mA cm}^{-2}$  over  $800 \text{ h}$ , as shown in Figure 3a. The typical magnified curve (Figure S10, Supporting Information) of the symmetric cell displays insignificant voltage fluctuation, indicative of the effective suppression of sodium dendrites growth. The result demonstrates the excellent compatibility between the PEGDMA-NaFSI-SPE and metallic sodium, which implies that the sodium anode with high specific capacity is suitable for this SPE-based high energy density ASSBs.

Electrochemical performances of the ASSB (NVP@C|PEGDMA-NaFSI-SPE|Na) were evaluated in the voltage

window of 2.8–3.8 V versus Na/Na<sup>+</sup> in soft-pack batteries at 60 °C. Figure 3b,c displays the rate performance and corresponding voltage profiles of the NVP@C|PEGDMA-NaFSI-SPE|Na at different current densities. It exhibits excellent reversible capabilities of 125, 116, 110, and 105 mAh g<sup>-1</sup> at 0.1, 0.2, 0.5, and 1 C (1 C = 120 mAh g<sup>-1</sup>), respectively. When the current density switches back to 0.1 C, a high reversible capacity of 123 mAh g<sup>-1</sup> still could be maintained. More impressively, the ASSB can deliver fairly high energy densities of 416, 388, 363, and 346 Wh kg<sup>-1</sup> at 0.1, 0.2, 0.5, and 1 C, respectively (the calculations of energy densities are based on the active materials mass in the cathode). According to the galvanostatic charge/discharge voltage profiles in Figure 3c, the NVP@C|PEGDMA-NaFSI-SPE|Na shows a typical two-phase reaction mechanism with a very flat potential plateau at around 3.38 V (versus Na/Na<sup>+</sup>) for charging process and 3.36 V (versus Na/Na<sup>+</sup>) for discharging process at 0.1 C, which corresponds to the V<sup>3+</sup>/V<sup>4+</sup> redox couple with two sodium extraction/insertion following this equation: Na<sub>3</sub>V<sub>2</sub>(PO<sub>4</sub>)<sub>3</sub> ↔ NaV<sub>2</sub>(PO<sub>4</sub>)<sub>3</sub>.<sup>[44]</sup> The NVP@C|PEGDMA-NaFSI-SPE|Na could exhibit low polarization voltages at around 2.8, 4.8, 9.3, and 15.9 mV at current densities of 0.1, 0.2, 0.5, and 1 C, respectively. The stable voltage plateau and low electrochemical polarization at various current densities indicate the superior conductivity and structural integrity of the electrode and electrolyte.<sup>[8]</sup> The long-term cycle was investigated at 0.5 C, as shown in Figure 3d. After the activation in the first few cycles, the NVP@C|PEGDMA-NaFSI-SPE|Na could deliver a high reversible capacity of 102 mAh g<sup>-1</sup> over 740 cycles (capacity decay of only 0.007% per cycle) with nearly 100% Coulombic efficiency. Moreover, the soft-pack ASSB could maintain 95% of the initial reversible capacity with almost no self-discharge even after resting for 3 months (inset in Figure 3d), demonstrating the excellent cycling stability and high capacity retention. Notably, the NVP@C|PEGDMA-NaFSI-SPE|Na in this work exhibits very comparable or even more outstanding electrochemical performances compared to recent reported solid-state sodium batteries (Table S1, Supporting Information).

The kinetic analysis of the NVP@C|PEGDMA-NaFSI-SPE|Na ASSB was further investigated by analyzing the cyclic voltammogram (CV) curves at various sweep rates of 0.02–0.12 mV s<sup>-1</sup> in the voltage window of 2.8–3.8 V by the Solartron 1470E electrochemical workstation (Figure 3e). The NVP@C|PEGDMA-NaFSI-SPE|Na exhibits very small potential polarization between cathodic and anodic peaks at the sweep rate of 0.02 mV s<sup>-1</sup>, indicating the superior ionic migration. With the sweep rate increasing from 0.02 to 0.12 mV s<sup>-1</sup>, a very slight shift in oxidation and reduction peaks can be observed, which further suggests the fast kinetics and weak polarization of this ASSB. Besides, the Na<sup>+</sup> diffusion coefficient (*D*<sub>Na</sub>) can be calculated according to the Randles-sevick equation as follows:

$$i_p = 2.69 \times 10^5 n^{3/2} A D_{Na}^{1/2} C_{Na} \nu^{1/2} \quad (2)$$

where *i*<sub>p</sub> represents the peak current, *A* stands for the surface area of electrode, *C*<sub>Na</sub> is the molar concentration of Na<sup>+</sup>, *n* is the number of transferred electrons, and *ν* is the sweep rate. Based on the fitted linear relationships between *i*<sub>p</sub> and *ν*<sup>1/2</sup> (Figure 3f),

the *D*<sub>Na</sub> values for Peak 1 (anodic) and Peak 2 (cathodic) are determined to be 4.07 × 10<sup>-11</sup> cm<sup>2</sup> s<sup>-1</sup> and 3.22 × 10<sup>-11</sup> cm<sup>2</sup> s<sup>-1</sup>, respectively, which are very close to those of previously reported NASICON-type liquid-electrolyte based SIBs, demonstrating the fast diffusion of Na<sup>+</sup> in the NVP@C|PEGDMA-NaFSI-SPE|Na ASSB.<sup>[51,52]</sup> Besides, the difference in kinetics between the anodic peak (Peak 1) and cathodic peak (Peak 2) can be analyzed by a power law equation, as follows:<sup>[53]</sup>

$$\log(i) = \log(a) + b \log(\nu) \quad (3)$$

where *i* is the peak current, *ν* is the scan rate, *a* and *b* are the fitting parameters. The *b* value reflects the reaction kinetics by estimating the ratio of capacitive-dominated charge storage of the electrode. The closer the *b*-value is to 1, the more prominent the capacitive behavior, which translates to a faster reaction kinetics.<sup>[53]</sup> The fitting curves in Figure 3g show an almost linear relationship. The *b* value of the NVP@C|PEGDMA-NaFSI-SPE|Na for anodic segment and cathodic segment is 0.67 and 0.64, respectively, indicating much faster kinetics of the anodic reaction process in the ASSB.<sup>[54]</sup>

To investigate the practical application of the soft-pack NVP@C|PEGDMA-NaFSI-SPE|Na in flexible electronic device, the bending measurement was conducted in the voltage window of 2.8–3.8 V versus Na/Na<sup>+</sup> at 60 °C (Figure 4). Schematic diagram of the bendable soft-pack ASSB is presented in Figure 4a, where the stage 1 and 3 represent the flat state and stage 2 is the folding state. The cycling performances of this soft-pack ASSB at different states are displayed in Figure 4b. It could achieve a very stable reversible capacity of around 106 mAh g<sup>-1</sup> (corresponding to energy density of ≈355 Wh kg<sup>-1</sup>) after 535 cycles at 0.5 C in both flat and folding state, which demonstrates its excellent flexibility and long cycle life under harsh conditions. In addition, the similar electrochemical impedance values of this soft-pack battery in flat state (52.1 Ω) and folding state (59.4 Ω) indicate the excellent interfacial contact between this SSE and the electrodes, which ensure the safety and stability of the bendable soft-pack ASSB under practical conditions (Figure 4c). Moreover, the evaluation of the bendable NVP@C|PEGDMA-NaFSI-SPE|Na battery under destructive conditions was further conducted at RT, as shown in Figure 4d–i and Figure S11a–c, Supporting Information. The LED device can function as usual under different bending conditions, indicating the excellent flexibility and safety of the bendable soft-pack ASSB.

To further figure out the prominent electrochemical performances of the NVP@C|PEGDMA-NaFSI-SPE|Na ASSBs, density functional theory (DFT) calculations were conducted to explore the Na<sup>+</sup> migration barrier in NVP configuration and PEGDMA-NaFSI-SPE configuration. The optimized models and paths of Na<sup>+</sup> migration of these two different structures are displayed in Figure 5a,b. The corresponding Na<sup>+</sup> diffusion energy barrier from Na1 to Na2 site is 0.28 and 0.19 eV for the NVP and PEGDMA-NaFSI-SPE configuration, respectively, according to the climbing-image nudged elastic band (cNEB) method.<sup>[54]</sup> The diffusion barriers of Na<sup>+</sup> in our ASSB system are much lower than many other reported electrode materials for SIBs, which is beneficial for fast reaction kinetics and superior electrochemical properties.<sup>[55]</sup>

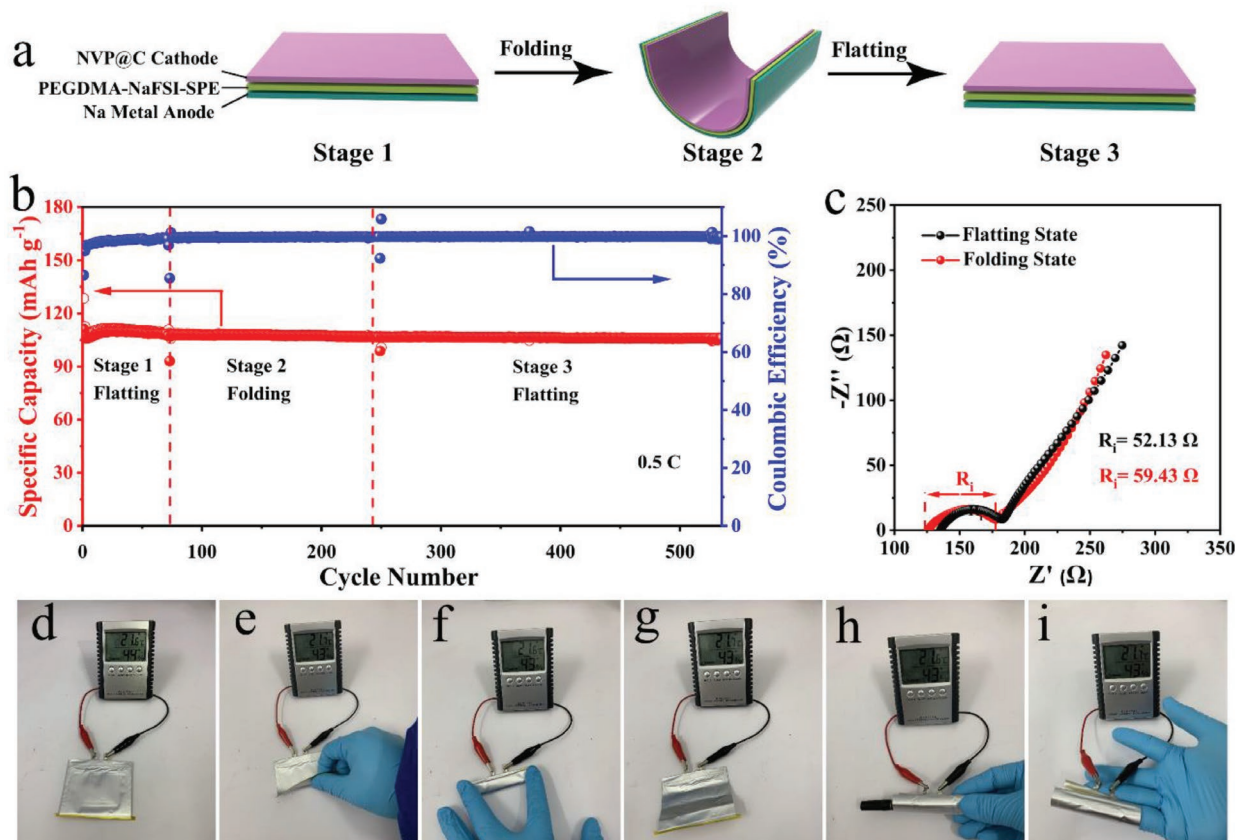


**Figure 4.** a) Schematic of the bendable NVP@C|PEGDMA-NaFSI-SPE|Na ASSB. b) Cycling performance and corresponding Coulombic efficiency at 0.5 C. c) Nyquist plots in flatting or folding state. d–i) Flexibility and safety evaluation under different conditions of the bendable soft-pack battery.

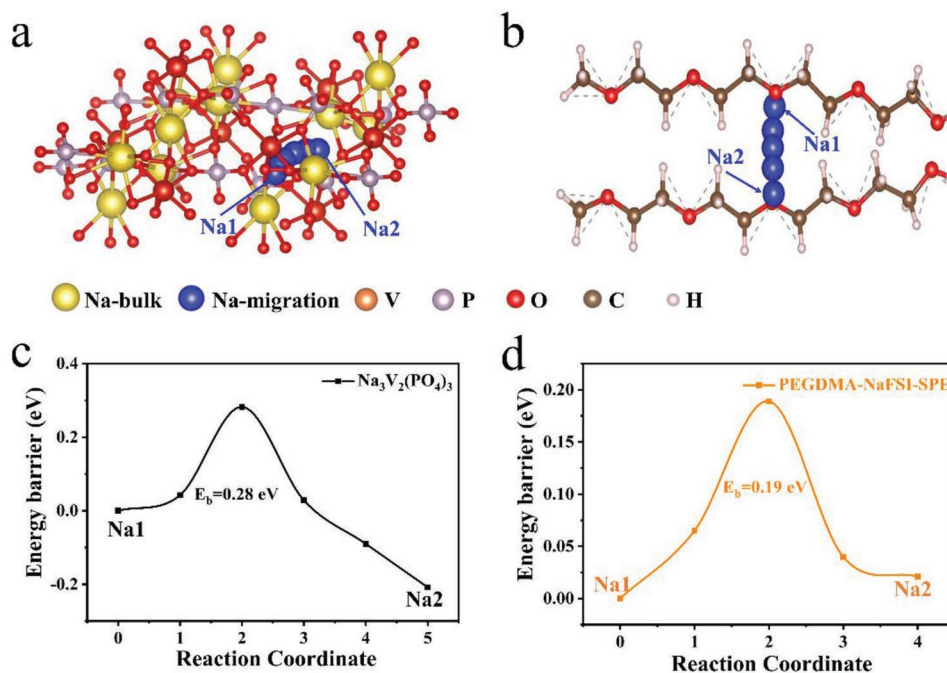


**Figure 5.** Schematic optimized crystal structure illustrating the optimum  $\text{Na}^+$  migration pathway of a) NVP configuration and b) PEGDMA-NaFSI-SPE configuration. The corresponding  $\text{Na}^+$  migration energy barrier from Na1 to Na2 site by the cNEB method in c) NVP configuration and d) PEGDMA-NaFSI-SPE configuration.

In summary, we have designed a high-performance all solid-state sodium battery (NVP@C|PEGDMA-NaFSI-SPE|Na) by employing the carbon-coated 3D interconnected flower-like NVP@C cathode, in situ synthesized solid polymer electrolyte (PEGDMA-NaFSI-SPE) and metallic sodium anode. The well-designed architecture of the ASSB system possesses the following advantages: 1) the highly efficient integrated system of SSE and electrode exhibits reduced interfacial resistance, enhanced mechanical flexibilities, and improved interfacial compatibility due to the good electrolyte/electrode solid-solid interface; 2) in situ solvent-free UV polymerization of the PEGDMA-NaFSI-SPE results in high ionic conductivity ( $\approx 10^{-4}$  S cm $^{-1}$  at RT) and significant resistance to dendrite growth; and 3) the carbon-coated 2D nanoplates assembled 3D flower-like structure of the NVP@C shortens the transport distance for Na $^{+}$ /electron and improves the electronic conductivity of the electrode materials. As a result, the advanced ASSB could exhibit excellent electrochemical properties, where high rate capacity of 105 mAh g $^{-1}$  is reached at 1.0 C and a capacity decay of 0.007% per cycle over 740 cycles at 0.5 C is also achieved in soft-pack batteries. More impressively, this ASSB exhibits almost no self-discharge behavior even after resting for 3 months. Besides, the bendable ASSB delivers a high energy density of 355 Wh kg $^{-1}$  after 535 cycles in flat state or folding state. The superior electrochemical performances can be attributed to the high diffusion coefficient and low diffusion energy barrier of Na $^{+}$  in the ASSB system, which are supported by the systematic experimental results and theoretical calculations. We believe this work may pave a new direction for fabricating high-performance flexible all solid-state sodium batteries.

## Supporting Information

Supporting Information is available from the Wiley Online Library or from the author.

## Acknowledgements

Y.Y. and Z.W. contributed equally to this work. This work was supported by National Key R&D Research Program of China (No. 2018YFB0905400), the National Natural Science Foundation of China (Nos. 51872283, 21805273, 51622210, 51872277, 51925207, and U1910210), the Fundamental Research Funds for the Central Universities (WK2060140026), Liaoning Revitalization Talents Program (Grant XLYC1807153), Natural Science Foundation of Liaoning Province, Joint Research Fund Liaoning-Shenyang National Laboratory for Materials Science (Grant 20180510038), DICP (DICP ZZBS201708, DICP ZZBS201802), DICP&QIBEBT (Grant DICP&QIBEBT UN201702), the DNL cooperation Fund, CAS (DNL180310, DNL180308, DNL201912, and DNL201915), Zhejiang Provincial Natural Science Foundation of China (No. LD18E020004, LY18E020018), Ningbo S&T Innovation 2025 Major Special Programme (No. 2018B10061, 2018B10087) and Youth Innovation Promotion Association CAS (2017342). The authors thank the USTC Super Computing Center for the computational resources.

## Conflict of Interest

The authors declare no conflict of interest.

## Keywords

Na $_3$ V $_2$ (PO $_4$ ) $_3$ , polymer electrolytes, solid-state sodium batteries, solvent-free

Received: November 10, 2019

Revised: December 21, 2019

Published online: January 30, 2020

- [1] B. Dunn, H. Kamath, J.-M. Tarascon, *Science* **2011**, *334*, 928.
- [2] J. Liu, *Adv. Funct. Mater.* **2013**, *23*, 924.
- [3] D. Larcher, J.-M. Tarascon, *Nat. Chem.* **2015**, *7*, 19.
- [4] C. Vaalma, D. Buchholz, M. Weil, S. Passerini, *Nat. Rev. Mater.* **2018**, *3*, 18013.
- [5] T. Matsuda, M. Takachi, Y. Moritomo, *Chem. Commun.* **2013**, *49*, 2750.
- [6] X. Xiang, K. Zhang, J. Chen, *Adv. Mater.* **2015**, *27*, 5343.
- [7] Z. Yu, S. L. Shang, J. H. Seo, D. Wang, X. Luo, Q. Huang, S. Chen, J. Lu, X. Li, Z. K. Liu, *Adv. Mater.* **2017**, *29*, 1605561.
- [8] C. Zhao, L. Liu, X. Qi, Y. Lu, F. Wu, J. Zhao, Y. Yu, Y. S. Hu, L. Chen, *Adv. Energy Mater.* **2018**, *8*, 1703012.
- [9] A. Hayashi, K. Noi, A. Sakuda, M. Tatsumisago, *Nat. Commun.* **2012**, *3*, 856.
- [10] W. Zhou, Y. Li, S. Xin, J. B. Goodenough, *ACS Cent. Sci.* **2017**, *3*, 52.
- [11] Z. Zhang, Q. Zhang, J. Shi, Y. S. Chu, X. Yu, K. Xu, M. Ge, H. Yan, W. Li, L. Gu, *Adv. Energy Mater.* **2017**, *7*, 1601196.
- [12] A. Banerjee, K. H. Park, J. W. Heo, Y. J. Nam, C. K. Moon, S. M. Oh, S. T. Hong, Y. S. Jung, *Angew. Chem., Int. Ed.* **2016**, *55*, 9634.
- [13] Y. Lu, L. Li, Q. Zhang, Z. Niu, J. Chen, *Joule* **2018**, *2*, 1747.
- [14] F. Mo, J. Ruan, S. Sun, Z. Lian, S. Yang, X. Yue, Y. Song, Y. N. Zhou, F. Fang, G. Sun, *Adv. Energy Mater.* **2019**, *9*, 1902123.
- [15] V. Thangadurai, S. Narayanan, D. Pinzar, *Chem. Soc. Rev.* **2014**, *43*, 4714.
- [16] A. Manthiram, X. Yu, S. Wang, *Nat. Rev. Mater.* **2017**, *2*, 16103.
- [17] Y. Kato, S. Hori, T. Saito, K. Suzuki, M. Hirayama, A. Mitsui, M. Yonemura, H. Iba, R. Kanno, *Nat. Energy* **2016**, *1*, 16030.
- [18] Q. An, F. Xiong, Q. Wei, J. Sheng, L. He, D. Ma, Y. Yao, L. Mai, *Adv. Energy Mater.* **2015**, *5*, 1401963.
- [19] C. Masquelier, *Nat. Mater.* **2011**, *10*, 649.
- [20] L. Porz, T. Swamy, B. W. Sheldon, D. Rettenwander, T. Frömling, H. L. Thaman, S. Berendts, R. Uecker, W. C. Carter, Y. M. Chiang, *Adv. Energy Mater.* **2017**, *7*, 1701003.
- [21] J. Zheng, M. Tang, Y. Y. Hu, *Angew. Chem., Int. Ed.* **2016**, *55*, 12538.
- [22] Z. Gao, H. Sun, L. Fu, F. Ye, Y. Zhang, W. Luo, Y. Huang, *Adv. Mater.* **2018**, *30*, 1705702.
- [23] D. Lei, Y.-B. He, H. Huang, Y. Yuan, G. Zhong, Q. Zhao, X. Hao, D. Zhang, C. Lai, S. Zhang, *Nat. Commun.* **2019**, *10*, 1.
- [24] L. Liu, X. Qi, S. Yin, Q. Zhang, X. Liu, L. Suo, H. Li, L. Chen, Y.-S. Hu, *ACS Energy Lett.* **2019**, *4*, 1650.
- [25] C. K. Moon, H.-J. Lee, K. H. Park, H. Kwak, J. W. Heo, K. Choi, H. Yang, M.-S. Kim, S.-T. Hong, J. H. Lee, *ACS Energy Lett.* **2018**, *3*, 2504.
- [26] H. Zhang, C. Li, M. Piszcz, E. Coya, T. Rojo, L. M. Rodriguez-Martinez, M. Armand, Z. Zhou, *Chem. Soc. Rev.* **2017**, *46*, 797.
- [27] J. Zhang, J. Zhao, L. Yue, Q. Wang, J. Chai, Z. Liu, X. Zhou, H. Li, Y. Guo, G. Cui, *Adv. Energy Mater.* **2015**, *5*, 1501082.
- [28] Q. Zhou, J. Ma, S. Dong, X. Li, G. Cui, *Adv. Mater.* **2019**, *31*, 1902029.
- [29] Z. Wei, Z. Zhang, S. Chen, Z. Wang, X. Yao, Y. Deng, X. Xu, *Energy Storage Mater.* **2019**, *22*, 337.
- [30] J. Yue, X. Zhu, F. Han, X. Fan, L. Wang, J. Yang, C. Wang, *ACS Appl. Mater. Interfaces* **2018**, *10*, 39645.

- [31] Y. Huang, L. Zhao, L. Li, M. Xie, F. Wu, R. Chen, *Adv. Mater.* **2019**, *31*, 1808393.
- [32] H. Gao, W. Zhou, K. Park, J. B. Goodenough, *Adv. Energy Mater.* **2016**, *6*, 1600467.
- [33] G. G. Eshetu, X. Judez, C. Li, M. Martinez-Ibañez, I. Gracia, O. Bondarchuk, J. Carrasco, L. M. Rodriguez-Martinez, H. Zhang, M. Armand, *J. Am. Chem. Soc.* **2018**, *140*, 9921.
- [34] L. Chen, Y. Li, S.-P. Li, L.-Z. Fan, C.-W. Nan, J. B. Goodenough, *Nano Energy* **2018**, *46*, 176.
- [35] S. B. Aziz, O. G. Abdullah, A. M. Hussein, R. T. Abdulwahid, M. A. Rasheed, H. M. Ahmed, S. W. Abdalqadir, A. R. Mohammed, *J. Mater. Sci.: Mater. Electron.* **2017**, *28*, 7473.
- [36] Y. Zhao, Z. Huang, S. Chen, B. Chen, J. Yang, Q. Zhang, F. Ding, Y. Chen, X. Xu, *Solid State Ionics* **2016**, *295*, 65.
- [37] Q. Ma, J. Liu, X. Qi, X. Rong, Y. Shao, W. Feng, J. Nie, Y.-S. Hu, H. Li, X. Huang, *J. Mater. Chem. A* **2017**, *5*, 7738.
- [38] L. Long, S. Wang, M. Xiao, Y. Meng, *J. Mater. Chem. A* **2016**, *4*, 10038.
- [39] D. Lei, K. Shi, H. Ye, Z. Wan, Y. Wang, L. Shen, B. Li, Q. H. Yang, F. Kang, Y. B. He, *Adv. Funct. Mater.* **2018**, *28*, 1707570.
- [40] Z. Wei, S. Chen, J. Wang, Z. Wang, Z. Zhang, X. Yao, Y. Deng, X. Xu, *J. Mater. Chem. A* **2018**, *6*, 13438.
- [41] C. Zhu, P. Kopold, P. A. van Aken, J. Maier, Y. Yu, *Adv. Mater.* **2016**, *28*, 2408.
- [42] Y. Jiang, X. Zhou, D. Li, X. Cheng, F. Liu, Y. Yu, *Adv. Energy Mater.* **2018**, *8*, 1800068.
- [43] Y. Fang, L. Xiao, X. Ai, Y. Cao, H. Yang, *Adv. Mater.* **2015**, *27*, 5895.
- [44] X. Rui, W. Sun, C. Wu, Y. Yu, Q. Yan, *Adv. Mater.* **2015**, *27*, 6670.
- [45] W. Ren, Z. Zheng, C. Xu, C. Niu, Q. Wei, Q. An, K. Zhao, M. Yan, M. Qin, L. Mai, *Nano Energy* **2016**, *25*, 145.
- [46] P. Hu, X. Wang, T. Wang, L. Chen, J. Ma, Q. Kong, S. Shi, G. Cui, *Adv. Sci.* **2016**, *3*, 1600112.
- [47] Y. Yao, Y. Jiang, H. Yang, X. Sun, Y. Yu, *Nanoscale* **2017**, *9*, 10880.
- [48] T. C. Nirmale, I. Karbhal, R. S. Kalubarme, M. V. Shelke, A. J. Varma, B. B. Kale, *ACS Appl. Mater. Interfaces* **2017**, *9*, 34773.
- [49] S. Chen, J. Wang, Z. Zhang, L. Wu, L. Yao, Z. Wei, Y. Deng, D. Xie, X. Yao, X. Xu, *J. Power Sources* **2018**, *387*, 72.
- [50] Z. Zhang, Y. Zhao, S. Chen, D. Xie, X. Yao, P. Cui, X. Xu, *J. Mater. Chem. A* **2017**, *5*, 16984.
- [51] X. Li, Y. Huang, J. Wang, L. Miao, Y. Li, Y. Liu, Y. Qiu, C. Fang, J. Han, Y. Huang, *J. Mater. Chem. A* **2018**, *6*, 1390.
- [52] J. Zhang, X. Zhao, Y. Song, Q. Li, Y. Liu, J. Chen, X. Xing, *Energy Storage Mater.* **2019**, *23*, 25.
- [53] Y. Yao, M. Chen, R. Xu, S. Zeng, H. Yang, S. Ye, F. Liu, X. Wu, Y. Yu, *Adv. Mater.* **2018**, *30*, 1805234.
- [54] Y. Yao, H. Wang, H. Yang, S. Zeng, R. Xu, F. Liu, P. Shi, Y. Feng, K. Wang, W. Yang, X. Wu, W. Luo, Y. Yu, *Adv. Mater.* **2019**, *1905658*, <https://doi.org/10.1002/adma.201905658>.
- [55] G. Henkelman, B. P. Uberuaga, H. Jónsson, *J. Chem. Phys.* **2000**, *113*, 9901.